

Facile electron delivery from graphene template to ultrathin metal-organic layers for boosting CO₂ photoreduction

Jia-Wei Wang

Sun Yat-Sen University <https://orcid.org/0000-0003-1966-7131>

Li-Zhen Qiao

Tianjin University of Technology

Haodong Nie

Soochow University

Hai-Hua Huang

Sun Yat-Sen University <https://orcid.org/0000-0002-1873-6871>

Yi Li

Soochow University

Shuang Yao

Tianjin University of Technology

Meng Liu

Tianjin University of Technology

Zhi-Ming Zhang (✉ zmzhang@email.tjut.edu.cn)

Tianjin University of Technology <https://orcid.org/0000-0003-3116-756X>

Zhenhui Kang

Soochow University

Tong-Bu Lu

Tianjin University of Technology

Article

Keywords: Metal-organic layers, heterogeneous catalysts, graphene oxide, photocatalysis

Posted Date: July 24th, 2020

DOI: <https://doi.org/10.21203/rs.3.rs-40766/v1>

License: © ⓘ This work is licensed under a Creative Commons Attribution 4.0 International License.

[Read Full License](#)

Version of Record: A version of this preprint was published at Nature Communications on February 5th, 2021. See the published version at <https://doi.org/10.1038/s41467-021-21084-9>.

Abstract

Metal-organic layers (MOLs) with ordered structure and molecular tunability are of great potential as heterogeneous catalysts due to their readily accessible active sites. Herein, we demonstrate a facile template strategy to prepare MOLs with a uniform thickness of three metal coordination layers (ca. 1.5 nm) with graphene oxide (GO) as both template and electron mediator. The resulting MOL@GO exhibits an outstanding performance for CO₂ photoreduction with a record-high total CO yield of 3133 mmol/gMOL among all the metal-organic framework and MOL catalysts (CO selectivity of 95%). This performance is ca. 34 times higher than that of bulky Co-MOF, [CoL(H₂O)₂]·0.5H₂O (H₂L = 5-(1H-1,2,4-triazol-1-yl)isophthalic acid). Systematic studies reveal that well exposed active sites in MOLs, and facile electron transfer between heterogeneous and homogeneous components mediated by GO, greatly contribute to its high activity. This work highlights a facile way for constructing ultrathin MOLs and demonstrate charge transfer pathway between conductive template and catalyst for boosting photocatalysis.

Introduction

Sunlight-driven CO₂ reduction has been regarded as a promising way to simultaneously achieve solar-to-chemical energy conversion and mitigate CO₂ pollution.^{1–3} Presently, solar-driven conversion of CO₂-to-chemical proceeds slowly as it requires the activation of thermodynamically stable CO₂ molecules and multiple electron/proton transfer processes. During the photocatalysis, various products, such as CO, CH₄, HCOOH, and methanol, usually generate simultaneously with low selectivity, and compete with H₂ evolution. To address these issues, metal-organic frameworks (MOFs), benefiting from their porous feature, ordered structure and molecular tunability, have been widely used to mediate photocatalytic CO₂ reduction.^{4–18} In this field, Lin et al,¹⁶ incorporated Re(CO)₃(bpy)Cl (bpy = bipyridine) modules into the UiO-67 framework, achieving a total turnover number (TON) of 10.9 in photocatalytic CO₂-to-CO conversion. Wang et al achieved a high TON of 450 by using a Co-based zeolitic imidazolate framework as the cocatalyst in the presence of [Ru(bpy)₃]²⁺ photosensitizer (PS).¹³ Lan et al introduced adenine moieties into cobalt-based MOFs to drive photocatalytic CO₂ reduction.⁸ Li and co-workers discovered that the amine-functionalization of linking units in a series of Fe-based MOFs can improve their photocatalytic performance for CO₂ reduction.¹⁵ Recently, perovskite quantum dots were introduced into MOF matrices to synergistically catalyze CO₂ photoreduction.^{17,18} For CO₂ reduction, great progress has been achieved with MOFs as low-cost catalysts. However, their performances were seriously hindered by the generally bulky nature with insufficient active sites and lethargic mass/charge transfer.

Nanosizing MOFs into ultrathin metal-organic layers (MOLs) can efficiently accelerate mass transport / electron transfer and create abundant readily accessible active sites to ensure high activity in various catalytic reactions.^{19–34} Moreover, ultrathin MOFs with limited number of atoms represent ideal models to explore structure-performance relationships for further rationally constructing efficient catalysts at

atomic/molecular levels. For example, a mono-carboxylic bipyridine ligand was utilized to assemble Re-/Mn-Ru molecules into monolayer Hf-based MOLs,²⁰ the resulting Re-Ru-based MOLs can sustainably reduce CO₂ to CO under real sunlight for one week. A two-step synthesis method was used for molecular tunability to construct Ni-based MOLs, which are competent for photoreduction of diluted CO₂.²¹ Up to date, a limited number of isolated MOLs can be synthesized due to their high surface energy and the serious lack of effective synthesis strategies. In principle, the MOLs can be stabilized by templates or surfactants to reduce the surface energy. However, these additional auxiliary components usually block the catalytic active sites to hinder efficient mass/charge transfer, thus severely reducing the catalytic activity. Therefore, rational design of ultrathin MOLs with functional substrates to integrate their advantages for synergistic photocatalysis will represent a promising method for constructing stable and highly efficient photocatalysts, but still a challenging task.

Herein, we demonstrate a facile template strategy to prepare MOLs with a uniform thickness of three metal coordination layers (ca. 1.5 nm) by using graphene oxide (GO) as both template and electron mediator. In this composite, the conductive support not only can reduce the surface energy of the ultrathin nanosheets to isolate and stabilize the three-layer MOLs, but also can efficiently accelerate electron transfer during the CO₂-to-CO conversion, achieving a record high CO yield of 3133 mmol/g_{MOL}, ca. 34 times higher than that of bulky Co-MOF, much superior to those of all the state-of-the-art MOF and MOL catalysts.

Results

Synthesis and characterization

The bulky Co-MOF, [CoL(H₂O)₂]·0.5H₂O (H₂L = 5-(1*H*1,2,4-triazol-1-yl)isophthalic acid), was synthesized via a solvothermal reaction of CoCl₂·6H₂O and H₂L in DMF/H₂O at 130 °C for 72 h (see the Methods). Single-crystal X-ray diffraction analyses reveal that Co-MOF crystallizes in a monoclinic crystal system with a space group of *C*2/c (Supplementary Table 1). As shown in Figure 1a, the asymmetric unit of Co-MOF contains one Co²⁺ cation coordinated by two aqua ligands, one N donor from the triazine moiety as well as three O atoms from two independent carboxylate groups in two L ligands. Through this coordination mode, one cobalt center connects with three organic ligands into a plane parallel to *b* axis, forming a 2D layer-like structure. The 2D layers are stacked together via H-bonding interactions (O-H···O = 2.760(4) Å, Supplementary Figure 1) between aqua molecules and carboxylate oxygen atoms, showing negligible voids in the framework (Supplementary Figure 2).

Afterwards, the bulk phase purity of Co-MOF was confirmed by powder X-ray diffraction (PXRD; Figure 1b) by comparison with that simulated from single crystal data. Importantly, the sharp peak at 26.7° corresponding to (404(–)) face was found to represent the stacking direction of MOLs with a lattice spacing of 0.33 nm, consistent with the distance between two 2D planes. Tightly stacking among these 2D layers in Co-MOF results in the bulky crystals with sizes over 50 μm, which can only be transformed into ca. 2 μm crystals after ultrasonic treatment (Supplementary Figure 3). The close stacking will

inevitably decrease the exposed active sites and impede the mass transport / electron transfer during the photocatalysis.

To overcome these problems, we attempt to use GO as 2D template to graft and stabilize metal coordination layers of Co-MOF to construct ultrathin MOL nanosheets. The synthetic procedure includes the incorporation of Co^{2+} ions into GO and the subsequent in-situ growth of Co-MOLs with H_2L ligand on the 2D GO template (see Methods and Figure 1c). First, both the PXRD (Figure 1b) and FT-IR (Figure 1d) measurements on Co-MOF, GO and Co-MOL@GO samples reveal the effective graft of Co-MOL layers on the GO support. It should be noted that the peak of (404(–)) face at 26.7° is absent in the PXRD pattern of Co-MOL@GO (Figure 1b), indicating an obvious reduction of the stacking effect in MOLs on the GO support and the effective separation between different layers. The Co-MOL@GO sample contains approximately 6.9% Co-MOL moiety ($1.2\% \pm 0.02\%$ Co) determined by ICP-MS via repeated measurements.

Subsequently, the morphology of Co-MOL@GO was studied by transmission electron microscopy (TEM; Figure 1e), where small nanoflakes (15-20 nm) were homogeneously distributed on the GO template. EDS mapping images indicate the even distribution of Co, N, C and O elements on the Co-MOL@GO sample (Supplementary Figure 4). Atomic force microscopic (AFM) results also show the distribution of nanosheets on GO substrates (Figure 1f), with an average diameter of ca. 20 nm and a thickness of ca. 1.5 nm, close to three metal coordination layers of 1.4 nm determined by the single-crystal X-ray diffraction analysis (Figure 1a). Furthermore, high-resolution TEM (HRTEM; Figure 1g) measurements clearly show the crystal spacing of 0.27 nm in the tiny nanocrystal, in good agreement with the appearance of (040) facets, which is also consistent with the PXRD results with the characteristic peak located at 33.4° (0.27 nm) (Figure 1b). Accordingly, all the above experimental results can prove the successful immobilization of ultrathin Co-MOLs on the GO template, resulting in the Co-MOL@GO composite. Upon increasing the loading amount of Co^{2+} , larger size of 2D nanosheets can be observed on the GO substrate, as indicated by TEM and PXRD measurements (Supplementary Figure 5). These results further confirm that the GO template synthesis represents a facile strategy for the synthesis of ultrathin MOL nanosheets.

With the verified morphology of Co-MOL@GO, a series of additional measurements were operated to verify the changes of Co-MOLs and GO in Co-MOL@GO sample. Initially, X-ray photoelectron spectroscopy (XPS; Figure 2a) reveals a negative shift in the binding energies of Co 2p in Co-MOL@GO compared to those of Co-MOF. This observation indicates the existence of interactions between Co-MOF and GO surface, which can facilitate the charge transfer between Co-MOF and GO to impede the recombination of charge carriers.³⁵ Moreover, GO substrate was substantially reduced under the solvothermal condition, which was confirmed by the Raman spectra of Co-MOL@GO with an increased ratio between defective bands (I_D) and graphitic band (I_G) relative to that of GO (1.54 vs 1.33) (Figure 2b).³⁶ The reduced GO can be more conductive and feasible for electron transfer during photocatalytic process. This conclusion was further supported by the results of electrochemical impedance

spectroscopy (EIS), where Co-MOL@GO exhibits a smaller charge-transfer resistance compared to those of Co-MOF and GO (Figure 2c). Overall, all above results suggest that Co-MOL@GO can be a good candidate as a catalyst for photocatalytic CO₂ reduction with its advantages in abundantly exposed active sites, excellent mass transport and charge-transfer ability.

Photocatalytic CO₂ reduction

The catalytic performance of Co-MOL@GO for visible-light-driven ($\lambda = 450$ nm) CO₂ reduction was investigated in a CO₂-saturated CH₃CN/H₂O ($v:v = 4:1$) solution. Ru(phen)₃(PF₆)₃ (phen = 1,10-phenanthroline; denoted as RuPS) was employed as the PS. Co-MOF, Co@GO and GO were used as the catalysts in the control experiments. The gaseous products, CO and H₂, were analyzed by gas chromatography, and the liquid products, i.e. HCOOH, were checked by ion chromatography. As shown in Figure 3 and Table 1, the main products are CO and H₂, and no liquid products can be detected.

Remarkably, a CO yield of 216.2 mmol/g with a high selectivity of 95% can be achieved during 12 h irradiation of Co-MOL@GO-based photocatalytic system. In comparison, the photocatalytic experiment with bulky Co-MOF as the catalyst affords a CO yield of 91.5 mmol/g_{MOF}, much smaller than that of Co-MOL@GO-containing system, as well as a lower selectivity of 82%. Control experiments reveal that GO shows no activity towards CO₂ reduction under this photocatalytic condition, indicating that the MOLs should be the real active species in the Co-MOL@GO sample. As a result, the CO yield can be estimated as 3133 mmol/g_{MOL}, ca. 34 times higher than that of bulky Co-MOF under similar condition, indicative of the remarkable intrinsic catalytic activity of ultrathin Co-MOF in Co-MOL@GO. Impressively, in terms of CO yield and selectivity, the catalytic performance of Co-MOL@GO (3133 mmol/g_{MOL}, 95%) is superior to those of all the state-of-the-art MOF catalysts for visible-light-driven CO₂ reduction (Supplementary Table 2).³⁷ Additionally, the photocatalytic system with Co@GO as the catalyst can also produce CO and H₂ under the same conditions, but with a much smaller amount than that of Co-MOL@GO (Supplementary Figure 6), showing that the formation of Co-MOL nanosheets on GO is the key to achieve high-performance CO₂ reduction. Accordingly, GO template strategy is promising to fabricate high-performance catalysts for photocatalytic CO₂ reduction. These comparative results clearly demonstrate much-enhanced intrinsic catalytic activity of 2D-nanosized Co-MOL in contrast to the bulky Co-MOF and other samples. This enhancement can be mainly attributed to its great exposure of catalytic active sites enabled by the ultrathin feature of the MOL, and the incorporation of graphene as charge-transfer mediator.

Table 1 | Photocatalytic results for CO₂ reduction to CO.^a

Entry	Catalyst	CO Yield (mmol/g)	H ₂ Yield (mmol/g)	CO (%)
1	Co-MOL@GO	216.2 (3133) ^[b]	11.2 (162) ^[b]	95
2	Co-MOF	91.5	19.8	82
3	Co@GO	66.7	3.16	95
4	GO	N.D.	< 0.10 ^[c]	N.A.
5	No catalyst	N.D.	< 0.10 ^[c]	N.A.

^aConditions: CO₂ saturated 5.0 mL CH₃CN/H₂O (*v*:*v* = 4:1), catalyst (10 mg/L), RuPS (0.4 mM), TEOA (0.3 M), light intensity of 100 mW/cm² (λ = 450 nm), 12 h of irradiation. ^[b]Calculated based on Co-MOL moiety. ^[c]Near the detection limits.

Thermal and chemical stability of Co-MOF and Co-MOL@GO were carefully investigated. For Co-MOF, thermogravimetric analysis (TGA) was conducted to investigate its thermal stability. As shown in Supplementary Figure 7, the TGA curve shows three continuous weight losses from 95 to 320 °C, suggesting the loss of lattice and coordinated water molecules in the cavity of bulky Co-MOF. It could also be observed that a thermal decomposition of Co-MOF took place until heating up to 400 °C, revealing its high thermal stability. Meanwhile, the bulk Co-MOF was soaked in a CO₂-saturated CH₃CN/H₂O (*v*:*v* = 4 : 1) solution containing 0.3 M TEOA, a reaction medium for photocatalytic CO₂ reduction. After one day, the solid samples were isolated for subsequent PXRD measurements. No obvious difference of the PXRD pattern can be observed compared to that of as-synthesized sample (Supplementary Figure 8). These results demonstrate remarkable thermal and chemical stability of this Co-MOF, assuring its robustness in photocatalytic CO₂ reduction. For Co-MOL@GO, PXRD pattern of the solid sample isolated from the photocatalytic system shows similar signals with that of as-prepared Co-MOL@GO, indicating the intact crystalline composition of Co-MOL@GO catalyst after photocatalysis (Supplementary Figure 9). Moreover, recycle experiments show no substantial decrease in the activity after three runs of photocatalytic reactions, confirming the retained activity of the Co-MOL@GO catalyst (Figure 3b). On the other hand, isotope labeling experiment with ¹³CO₂ shows that ¹³CO is the main product in this photocatalytic system (Figure 3c), manifesting that the CO product really derives from CO₂ rather than the decomposition of TEOA, RuPS, GO or Co-MOLs. All these results demonstrate the excellent stability of Co-MOL@GO in the photocatalytic CO₂-to-CO conversion.

Electron transfer pathway

To elucidate the electron transfer pathway, the emission quenching experiments of RuPS were conducted in detail with the quenchers including Co-MOL@GO, Co-MOF and TEOA (Figure 3d-3e and Supplementary Figure 10). In the fluorescence spectra of RuPS, an emission peak at 598 nm was detected with the excitation at 450 nm. Upon the gradual addition of Co-MOL@GO, the efficiency of fluorescence quenching was far higher than those obtained by addition of bulky Co-MOF and GO, indicating that the ultrathin feature of MOL and the incorporation of graphene mediator are beneficial to electron transfer. The K_{sv} quenching constants of RuPS quenched by Co-MOL@GO was calculated as 3250 L g⁻¹ by Stern-Volmer

plot,^{38,39} much higher than that obtained by addition of Co-MOF (813 L g^{-1}), and no obvious quenching can be observed in the presence of isolated GO. These results suggest the fast electron transfer between homogeneous PS* and heterogeneous Co-MOL@GO catalyst mediated by GO, affording the high catalytic performance.^{38,39} Further, control experiments show that negligible fluorescent quenching can be detected by addition of various amounts of TEOA (Figure 3e), indicating that the exited RuPS* was directly quenched by Co-MOL@GO via an oxidation quenching mechanism.

The acceleration of charge transfer was confirmed by time-resolved absorption spectroscopy. As shown in Figure 3f, the kinetic traces for excited RuPS show that the lifetime of RuPS* (478.3 ns) was much longer than that obtained in the presence of Co-MOF (412.7 ns) catalyst, and this lifetime can be further shortened to be 357.0 ns when Co-MOL@GO composite was present. These results suggest the rapid separation and migration of photogenerated charge carriers between homogeneous PS and heterogeneous catalyst with graphene as the mediator. In the presence of TEOA, the excited lifetime of RuPS* was similar to that of isolated RuPS (481.9 vs. 478.3 ns), further confirming the oxidative quenching electron transfer pathway in this photocatalytic reaction for CO_2 reduction.⁴⁰

Further, the acceleration of electron transfer mediated by GO and the roles of different components in the photocatalytic system were evaluated by *in situ* transient photovoltage (TPV) measurements on GO, Co-MOF, RuPS, and Co-MOL@GO. As shown in Figure 4a, the photocurrent response of GO is the highest among the detected samples, and its curve in the $\text{CH}_3\text{CN}/\text{H}_2\text{O}$ ($v:v = 4:1$) medium is similar to that in the air (Supplementary Figure 11). Figure 4b shows that the photocurrent intensity of Co-MOF/RuPS mixture is higher than that of isolated components of Co-MOF and RuPS. These results suggest a coupling effect between Co-MOF and RuPS that can enhance the signal, while the response of GO is still stronger than that of Co-MOF/RuPS (Figure 4c). Then, the photocurrent intensity decreased when GO was mixed with RuPS or Co-MOF (Co-MOL), respectively. Especially, the photocurrent intensity of Co-MOL@GO composite is much lower than that from the combination of GO and RuPS (Figure 4d). These observations infer the electron transfer pathway, in which the electrons can be transferred to both Co-MOL and RuPS from the GO surface, and Co-MOL can accept electrons more easily than RuPS.

To determine the active centers, the TPV measurements were performed in different atmospheres of N_2 and CO_2 to evaluate the real catalytic active centers (Figure 4e-4h). As shown in Figure 4e and 4f, similar photocurrent intensities were observed in the curves of either GO or RuPS under N_2 or CO_2 . In contrast, a sharp decrease of photocurrent intensity was detected with Co-MOF under CO_2 in comparison with that under N_2 (Figure 4g). These results reveal that the photocatalytic CO_2 reduction should occur on the surface of Co-MOF. That is, Co-MOL represents the active component in the system. To further confirm this proposal, the TPV of Co-MOL@GO/RuPS mixture was performed, and a similar trend to that of Co-MOF was observed, confirming the role of Co-MOL as the active center (Figure 4h). Overall, the above TPV analyses confirm that Co-MOL is the active component of photocatalytic CO_2 reduction and that GO serves as the electron mediator to deliver electrons to Co-MOL.

Mechanistic studies

As the Co-MOL is the active component in photocatalysis, its molecular catalytic mechanism was further investigated by the electrochemical measurements. First, we studied the electrochemical behavior of GO and Co-MOL@GO loaded on the surface of the glassy carbon electrode (GCE), respectively. As shown in Supplementary Figure 12a, the irreversible waves at ca. -0.75 V versus normal hydrogen electrode (vs. NHE) were both observed in the cyclic voltammograms (CVs) of Co-MOL@GO and GO under N₂, where the reduction currents are mainly attributed to the reduction events at GO. To avoid the interference of GO, Co-MOF was directly employed to investigate the redox behavior of the MOF catalyst. As shown in Supplementary Figure 12b, a quasi-reversible redox couple at $E_{1/2} = -0.76$ V vs. NHE (reduction wave at -0.85 V) appeared in the CV of Co-MOF under N₂, corresponding to Co^{II/1} reduction. Upon purging CO₂ into the system, an irreversible reduction wave peaking at -0.94 V vs. NHE with a relatively large current was detected, indicating a chemical step driven by Co^{II/1} reduction, most possibly for catalytic CO₂ reduction,⁴¹ as the position of this reduction wave is more negative than the standard reduction potential of CO₂/CO (-0.65 V vs. NHE).⁴² Moreover, the above results indicate that the catalysis driven by the photoexcited RuPS* should be thermodynamically accessible, as the driving force from the oxidative quenching pathway ($E = -0.84$ V vs. NHE)⁴³ is more negative than the onset potential (ca. -0.75 V) of the catalytic wave.

According to above studies,^{41,44} the catalytic mechanism of Co-MOF in CO₂-to-CO conversion can be tentatively proposed, which was further verified by DFT calculation. A molecular prototype presenting the Co-complex moiety was subjected in computational studies (Figure 5a). The overall free energy changes are downhill besides the rate-determining CO₂-binding step, suggesting the calculated catalytic cycle is theoretically viable. As illustrated by Figure 5, the photocatalytic cycle begins with the photo-excitation of RuPS (Figure 5b). Then, the excited RuPS* species can be oxidatively quenched by Co-MOL@GO catalyst to drive the Co^{II/1} reduction to form Co^I species. The calculated potential for the reduction from Co^{II} to Co^I is -1.03 V vs. NHE, approaching to the measured value (ca. -0.94 V) in the presence of CO₂, further confirming the accessibility of this proposed mechanism. The Co^I intermediate can react with CO₂ to generate a Co-CO₂ adduct. Then a 1e⁻/1H⁺ proton-coupled electron transfer takes place to generate a Co-COOH species. The reduction and protonation from Co-CO₂ to Co-COOH is also viable as the calculated reduction potential (+0.39 V) is much more positive than the Co^{II/1} reduction potential. Finally, the C-OH bond in the Co-COOH intermediate will cleave and release CO to recover the Co^{II} state. The remaining RuPS⁺ species from the oxidative quenching pathway can be reduced to original RuPS by the TEOA, completing the photocatalytic cycle. During this photocatalytic process, the 2D GO not only serves as the template to reduce the surface energy of ultrathin nanosheets for constructing ultrathin MOLs with more exposed active sites, but also to supply conductive channels that can facilitate photoexcited electron transfer, which both play key roles in promoting the photocatalysis.

Discussion

In summary, we have developed a facile and efficient strategy to construct ultrathin 2D MOLs with three metal coordination layers, where the MOLs are homogeneously distributed on the 2D GO template. The synergy between ultrathin MOL and the GO electronic conductor can greatly improve its intrinsic activity for photocatalytic CO₂ reduction. The reduced GO can act as 2D template to support and stabilize the MOLs in a uniform thickness of ca. 1.5 nm. Importantly, the GO can serve as efficient electron mediator to bridge the gap between heterogeneous catalysts and homogeneous antenna molecules, greatly contributing to the extremely high activity. By merging these advantages, Co-MOL@GO exhibits excellent catalytic activity and high selectivity towards visible-light-driven CO₂-to-CO conversion, achieving a record-high total CO yield of 3133 mmol/g_{MOL} in 12 h among all the state-of-the-art MOF and MOL catalysts. This work paves a new avenue on the economical preparation of ultrathin MOLs with advanced performance and demonstrates the key role of the electron mediator in dramatically promoting the photocatalysis.

Methods

Materials

All the chemicals, commercially available, were used without further purification. The used water was prepared by using a Milli-Q ultrapure water purification system. Electrodes and other accessories were all purchased from Gauss Union Technology Co., Ltd.

Instruments

PXRD data were collected by a Smart X-ray diffractometer (SmartLab 9 KW, Rigaku, Japan) with Cu Ka radiation ($\lambda = 1.54178 \text{ \AA}$). EDS mapping images were acquired on an Environment Scanning Electron Microscope with a field emission gun (Quanta FEG 250, FEI, America). The morphologies were recorded by a scanning electron microscope (Verios 460L, FEI, America) and a transmission electron microscope (Talos F200 X, FEI, America). The Co contents were determined by ICP-MS (iCAP RQ, Germany). Raman spectra were recorded on a high-resolution laser confocal fiber Raman spectrometer (HORIBA EVOLVTION, HORIBA Jobinyvon, France). More elemental information, especially for their valence states, was determined by XPS (ESCALAB250Xi, THERMO SCIENTIFIC, United Kingdom). The evolved CO and H₂ were monitored by using an Agilent 7820A gas chromatography or a Shimadzu GC-2014 gas chromatography. The fluorescent spectra were conducted on a fluorescence spectrophotomer (F-7000, Hitachi, Japan). Time-resolved fluorescence measurements were measured with MicroTime 200 time-resolved confocal fluorescence instrument. The experimental data was analyzed by the SymPhoTime 64. Electrochemical measurements were operated on a CHI660D work station.

Synthesis of Co-MOL@GO

The first step is the immobilization of Co²⁺ on the 2D GO nanosheets. The GO was synthesized according to previous report.^{45,46} 20 mg GO and 0.5 mL water were added into 25 mL ethanol to obtain a

homogeneous suspension after 1 h of ultrasonic treatment. Then, 0.5 mL aqueous solution of $\text{CoCl}_2 \cdot 6\text{H}_2\text{O}$ (0.1 M) was added into this GO suspension. After reaction at 80 °C for 24 h, the resulting Co@GO ($4.98 \pm 0.06\%$ Co, determined by ICP-MS) powder was isolated by centrifugation, followed by washing with water for several times and drying at 60 °C. The second step is the growth of Co-MOL on the GO layers. Co@GO (20 mg) and 5-(1*H*1,2,4-triazol-1-yl)isophthalic acid (10 mg) were added into a mixed solvent of 1.75 mL DMF, 0.5 mL water and 0.25 mL acetic acid in a 10 mL Teflon-lined autoclave. After reaction at 130 °C for 4 h, the Co-MOL@GO sample was obtained, which was washed by water and ethanol, followed by drying at 60 °C. For the larger-sized Co-MOLs on the GO, it was synthesized under the similar conditions except using 1.0 mL aqueous solution of $\text{CoCl}_2 \cdot 6\text{H}_2\text{O}$ (0.1 M).

Synthesis of Co-MOF

In a 10 mL Teflon-lined autoclave, $\text{CoCl}_2 \cdot 6\text{H}_2\text{O}$ (18.0 mg) and 5-(1*H*1,2,4-triazol-1-yl)isophthalic acid (9.0 mg) were dissolved in a mixed solvent containing 1.75 mL DMF, 0.5 mL water and 0.25 mL acetic acid. After a 72-h reaction under 130 °C, this mixture afforded violet crystals of Co-MOF, which were cleansed by water and ethanol, followed by drying at 60 °C.

X-ray crystallography

Single-crystal X-ray diffraction data was collected by an X-ray single crystal diffractometer (XtaLAB Pro MM003Cu/Mo, Rigaku, Japan) equipped with Cu K α radiation ($\lambda = 1.54178 \text{ \AA}$). The structure was resolved using the direct method and refined on F^2 by the full-matrix least-squares method,⁴⁷ which yields the positions of all non-hydrogen atoms and were all refined anisotropically. All hydrogen atoms of the ligand were placed in their calculated positions with fixed isotropic thermal parameters and included in the structure factor calculations in the final stage of refinement. The crystallographic data was supplied in Supplementary Table 2. CCDC 1965944 contains the supplementary crystallographic data for this paper. The data can be obtained free of charge from The Cambridge Crystallographic Data Centre via <http://www.ccdc.cam.ac.uk/>.

EIS measurements

EIS measurements were conducted on a CHI660D electrochemical station in a conventional three-electrode cell using a Pt plate as the counter electrode and an Ag/AgCl electrode (saturated KCl) as the reference electrode. The working electrode was a catalyst-loaded fluorine-doped tin oxide (FTO) glass slide. Prior to catalyst coating, the FTO slides were cleaned by sonication in ethanol for 30 min and dried at 353 K. The boundary of the FTO glass was protected by using Scotch tape. Then, 2 mg of catalyst was dispersed in 200 μL of ethanol with 10 μL 5% Nafion solution by sonication for 1 h to obtain a slurry, which was drop-cast onto the cleaned FTO glass. After drying overnight, the working electrode was further dried at 393 K for 5 h to improve the adhesion. EIS measurements were carried out at the open circuit potential. Prior to all measurements, the electrolyte (0.2 M Na_2SO_4 aqueous solution) was purged with Ar.

Photocatalytic experiments

The photocatalytic reduction of CO₂ to CO was conducted in a 17 mL home-made reactor containing catalyst, [Ru(phen)₃](PF₆)₂, TEOA and CH₃CN/H₂O (*v:v* = 4:1) solution under 1 atm CO₂ atmosphere at 293±2 K. After purging CO₂ into this reaction system for 10 min, the photocatalytic reaction was initiated by irradiation of a blue LED (λ = 450 nm, light intensity = 100 mW/cm², irradiated area is approximate 0.5 cm²). The generated gases in the headspace were analyzed by a gas chromatography, and the possible products in the solution were analyzed by an ion chromatograph. Each photocatalytic reaction was repeated three times to confirm the reliability of the data.

In situ TPV measurements

The working electrodes (1 cm × 2 cm) were prepared by depositing samples (150 μ L 5 mg·mL⁻¹, dispersion liquid: 62.5% water, 25% isopropanol and 12.5% 5w% Nafion solution) on indium-tin oxide (ITO) glass substrates. During the testing process, the working electrodes were kept dry or wet with N₂ or CO₂ saturated CH₃CN/H₂O (*v:v* = 4:1), respectively. The samples were excited by a laser radiation pulse (λ = 355 nm, pulse width = 5 ns) from a third-harmonic Nd: YAG laser (Polaris II, New Wave Research, Inc.). The photocurrent is the ratio of the photovoltage to the internal resistance of the test systems.

Cyclic voltammetry

Cyclic voltammetric measurements were conducted on a CHI660D electrochemical station in a conventional three-electrode cell using a Pt wire as the counter electrode and another Pt wire as the pseudo reference electrode. Ferrocene (Fc) was added and its reversible couple served as the internal potential reference (vs. Fc^{+/Fc}), which was then converted to vs. NHE by adding 0.64 V.⁴¹ Catalyst-loaded glassy carbon disk electrode with 3 mm diameter was used as the working electrode. Prior to catalyst coating, the working electrode was polished by alumina oxide powder (50 nm) for 5 min and then cleaned by sonication in ethanol for 2 min, followed by drying in air at room temperature. Then, 5 mg of catalyst was dispersed in 4.95 mL of ethanol with 50 μ L 5% Nafion solution by sonication for 1 h to obtain a slurry. 2 μ L of the prepared slurry was then drop-cast onto the cleaned electrode and drying under ambient conditions for 2 h. The supporting electrolyte is wet CH₃CN containing tetra-*n*-butylammonium hexafluorophosphate (0.1 M).

DFT calculation

All the calculations were performed with Gaussian 09 program.⁴⁸ All the structures were optimized at the B3P86^{49,50}/def2SVP level of theory. Based on the crystal structure, some atoms were frozen during the optimizations. Frequency analysis calculations were performed to characterize the structures to be the minima. With B3P86/def2SVP optimized geometries, the energy results were refined by single-point calculations at the B3P86/def2TZVP level of theory. The solvation effect was also evaluated with the

SMD solvent model at the B3P86/def2TZVP level of theory. For the redox potentials calculation, the result was calculated by,

$$nE^\ominus F = \Delta G_{(sol)}^\ominus$$

where $\Delta G_{(solv)}^\ominus$ is the free energy change of the reduction process at standard conditions, n is the number of electrons, F is the Faraday constant. According to the experimental $\text{Fc}^{+/0}$ couple value of -114.8 kcal/mol (-4.98 V)⁵¹ in CH_3CN , the calculated redox potentials are referenced to $\text{Fc}^{+/0}$ by subtracting 4.98 V, then converting to versus NHE by adding 0.64 V.

Declarations

Data availability

Supplementary Figures are available from the authors.

Acknowledgments

This work was supported by National Natural Science Foundation of China (21722104, 21671032 and 21971190), Natural Science Foundation of Tianjin City of China (18JCJQJC47700), and the Fundamental Research Funds for the Central Universities (20lgpy87).

Author contributions

Z.M.Z conceived and designed this project, J.W.W, L.Z.Q, H.D.N, Y.L and M.L performed the experiments, H.H.H carried out the DFT calculation, J.W.W, Y.S, Z.H.K, Z.M.Z, Z.H.K and T.B.L analyzed the data, J.W.W, Z.H.K and Z.M.Z wrote and revised the article. All authors participated in drafting the paper, and gave approval to the final version of the manuscript.

Competing Interests

The authors declare no competing interests.

References

1. Peter, S. C. Reduction of CO_2 to chemicals and fuels: A solution to global warming and energy crisis. *ACS Energy Lett.* **3**, 1557–1561 (2018).
2. Zhang, H. X., et al. Isolated square-planar copper center in boron imidazolate nanocages for photocatalytic reduction of CO_2 to CO. *Angew. Chem. Int. Ed.* **58**, 11752–11756 (2019).
3. Guo, Q., et al. Efficient and selective CO_2 reduction integrated with organic synthesis by solar energy. *Chem* **5**, 2605–2616 (2019).

4. Kuppler, R. J., *et al.* Potential applications of metal-organic frameworks. *Coord. Chem. Rev.* **253**, 3042–3066 (2009).
5. Furukawa, H., Cordova, K. E., O'Keeffe, M. & Yaghi, O. M. The chemistry and applications of metal-organic frameworks. *Science* **341**, 1230444 (2013).
6. Muschi, M., *et al.* Formation of a single-crystal aluminum-based MOF nanowire with graphene oxide nanoscrolls as structure-directing agents. *Angew. Chem. Int. Ed.* **59**, 10353–10358 (2020).
7. Alkhatib, I. I., Garlisi, C., Pagliaro, M., Al-Ali, K. & Palmisano, G. Metal-organic frameworks for photocatalytic CO₂ reduction under visible radiation: A review of strategies and applications. *Catal. Today* **340**, 209–224 (2020).
8. Li, N., *et al.* Adenine components in biomimetic metal-organic frameworks for efficient CO₂ photoconversion. *Angew. Chem. Int. Ed.* **58**, 5226–5231 (2019).
9. Jing, X., He, C., Zhao, L. & Duan, C. Photochemical properties of host-guest supramolecular systems with structurally confined metal-organic capsules. *Acc. Chem. Res.* **52**, 100–109 (2019).
10. Wang, Y., Huang, N. Y., Shen, J. Q., Liao, P. Q., Chen, X. M. & Zhang, J. P. Hydroxide ligands cooperate with catalytic centers in metal-organic frameworks for efficient photocatalytic CO₂ reduction. *J. Am. Chem. Soc.* **140**, 38–41 (2018).
11. Kajiwara, T., *et al.* Photochemical reduction of low concentrations of CO₂ in a porous coordination polymer with a ruthenium(II)-CO complex. *Angew. Chem. Int. Ed.* **55**, 2697–2700 (2016).
12. Zhang, H., *et al.* Efficient visible-light-driven carbon dioxide reduction by a single-atom implanted metal-organic framework. *Angew. Chem. Int. Ed.* **55**, 14310–14314 (2016).
13. Wang, S., Yao, W., Lin, J., Ding, Z. & Wang, X. Cobalt imidazolate metal-organic frameworks photosplit CO₂ under mild reaction conditions. *Angew. Chem. Int. Ed.* **53**, 1034–1038 (2014).
14. Li, D., Kassymova, M., Cai, X., Zang, S.-Q. & Jiang, H.-L. Photocatalytic CO₂ reduction over metal-organic framework-based materials. *Coord. Chem. Rev.* **412**, 213262 (2020).
15. Wang, D., Huang, R., Liu, W., Sun, D. & Li, Z. Fe-based MOFs for photocatalytic CO₂ reduction: Role of coordination unsaturated sites and dual excitation pathways. *ACS Catal.* **4**, 4254–4260 (2014).
16. Wang, C., Xie, Z., deKrafft, K. E. & Lin, W. Doping metal-organic frameworks for water oxidation, carbon dioxide reduction, and organic photocatalysis. *J. Am. Chem. Soc.* **133**, 13445–13454 (2011).
17. Wu, L. Y., *et al.* Encapsulating perovskite quantum dots in iron-based metal-organic frameworks (MOFs) for efficient photocatalytic CO₂ reduction. *Angew. Chem. Int. Ed.* **58**, 9491–9495 (2019).
18. Kong, Z. C., *et al.* Core@shell CsPbBr₃@zeolitic imidazolate framework nanocomposite for efficient photocatalytic CO₂ reduction. *ACS Energy Lett.* **3**, 2656–2662 (2018).
19. Xiao, X., Zou, L., Pang, H. & Xu, Q. Synthesis of micro/nanoscaled metal-organic frameworks and their direct electrochemical applications. *Chem. Soc. Rev.* **49**, 301–331 (2020).
20. Lan, G., *et al.* Photosensitizing metal-organic layers for efficient sunlight-driven carbon dioxide reduction. *J. Am. Chem. Soc.* **140**, 12369–12373 (2018).

21. Han, B., *et al.* Nickel metal-organic framework monolayers for photoreduction of diluted CO₂: Metal-node-dependent activity and selectivity. *Angew. Chem. Int. Ed.* **57**, 16811–16815 (2018).
22. Yang, L., *et al.* Two-dimensional metal-organic layers on carbon nanotubes to overcome conductivity constraint in electrocatalysis. *ACS Appl. Mater. Interfaces* **10**, 36290–36296 (2018).
23. Zhu, W., *et al.* Selective reduction of CO₂ by conductive MOF nanosheets as an efficient co-catalyst under visible light illumination. *Appl. Catal. B-Environ* **238**, 339–345 (2018).
24. Ye, L., *et al.* Assembly of highly efficient photocatalytic CO₂ conversion systems with ultrathin two-dimensional metal-organic framework nanosheets. *Appl. Catal. B-Environ* **227**, 54–60 (2018).
25. Zhuang, L., *et al.* A surfactant-free and scalable general strategy for synthesizing ultrathin two-dimensional metal-organic framework nanosheets for the oxygen evolution reaction. *Angew. Chem. Int. Ed.* **58**, 13565–13572 (2019).
26. Guo, Y., *et al.* Cooperative stabilization of the [pyridinium-CO₂-CO] adduct on a metal-organic layer enhances electrocatalytic CO₂ reduction. *J. Am. Chem. Soc.* **141**, 17875–17883 (2019).
27. Lin, Z., *et al.* Metal-organic layers stabilize earth-abundant metal-terpyridine diradical complexes for catalytic C-H activation. *Chem. Sci.* **9**, 143–151 (2018).
28. Shi, W., *et al.* Surface modification of two-dimensional metal-organic layers creates biomimetic catalytic microenvironments for selective oxidation. *Angew. Chem. Int. Ed.* **56**, 9704–9709 (2017).
29. Li, F. L., *et al.* Large-scale, bottom-up synthesis of binary metal-organic framework nanosheets for efficient water oxidation. *Angew. Chem. Int. Ed.* **58**, 7051–7056 (2019).
30. Han, J., *et al.* Reordering d orbital energies of single-site catalysts for CO₂ electroreduction. *Angew. Chem. Int. Ed.* **58**, 12711–12716 (2019).
31. Zhao, S., *et al.* Ultrathin metal-organic framework nanosheets for electrocatalytic oxygen evolution. *Nat. Energy* **1**, 16184 (2016).
32. Huang, J., *et al.* Electrochemical exfoliation of pillared-layer metal-organic framework to boost the oxygen evolution reaction. *Angew. Chem. Int. Ed.* **57**, 4632–4636 (2018).
33. Wu, H., *et al.* Mxene derived metal-organic frameworks. *J. Am. Chem. Soc.* **141**, 20037–20042 (2019).
34. Ding, Y., *et al.* Controlled intercalation and chemical exfoliation of layered metal-organic frameworks using a chemically labile intercalating agent. *J. Am. Chem. Soc.* **139**, 9136–9139 (2017).
35. Pan, Z., Zhang, G. & Wang, X. Polymeric carbon nitride/reduced graphene oxide/Fe₂O₃: All-solid-state Z-scheme system for photocatalytic overall water splitting. *Angew. Chem. Int. Ed.* **58**, 7102–7106 (2019).
36. Zhou, D., Cui, Y., Xiao, P. W., Jiang, M. Y. & Han, B. H. A general and scalable synthesis approach to porous graphene. *Nat. Commun.* **5**, 4716 (2014).
37. Niu, K., *et al.* A spongy nickel-organic CO₂ reduction photocatalyst for nearly 100% selective CO production. *Sci. Adv.* **3**, e1700921 (2017).

38. Bonin, J., Robert, M. & Routier, M. Selective and efficient photocatalytic CO₂ reduction to CO using visible light and an iron-based homogeneous catalyst. *J. Am. Chem. Soc.* **136**, 16768–16771 (2014).
39. Ouyang, T., Huang, H.-H., Wang, J.-W., Zhong, D.-C. & Lu, T.-B. A dinuclear cobalt cryptate as a homogeneous photocatalyst for highly selective and efficient visible-light driven CO₂ reduction to CO in CH₃CN/H₂O solution. *Angew. Chem. Int. Ed.* **56**, 738–743 (2017).
40. Chan, S. L., Lam, T. L., Yang, C., Yan, S. C. & Cheng, N. M. A robust and efficient cobalt molecular catalyst for CO₂ reduction. *Chem. Commun.* **51**, 7799–7801 (2015).
41. Wang, J.-W., Huang, H.-H., Sun, J.-K., Ouyang, T., Zhong, D.-C. & Lu, T.-B. Electrocatalytic and photocatalytic reduction of CO₂ to CO by cobalt(II) tripodal complexes: Low overpotentials, high efficiency and selectivity. *ChemSusChem* **11**, 1025–1031 (2018).
42. Costentin, C., Drouet, S., Robert, M. & Saveant, J. M. A local proton source enhances CO₂ electroreduction to CO by a molecular Fe catalyst. *Science* **338**, 90–94 (2012).
43. Ouyang, T., et al. Dinuclear metal synergistic catalysis boosts photochemical CO₂-to-CO conversion. *Angew. Chem. Int. Ed.* **57**, 16480–16485 (2018).
44. Wang, J.-W., Huang, H.-H., Sun, J.-K., Zhong, D.-C. & Lu, T.-B. Syngas production with a highly-robust nickel(II) homogeneous electrocatalyst in a water-containing system. *ACS Catal.* **8**, 7612–7620 (2018).
45. Hummers, W. S. & Offeman, R. E. Preparation of graphitic oxide. *J. Am. Chem. Soc.* **80**, 1339–1339 (1958).
46. Kovtyukhova, N. I., et al. Layer-by-layer assembly of ultrathin composite films from micron-sized graphite oxide sheets and polycations. *Chem. Mater.* **11**, 771–778 (1999).
47. Sheldrick, G. M. Crystal structure refinement with SHELXTL. *Acta Crystallogr., Sect. C: Struct. Chem.* **71**, 3–8 (2015).
48. Frisch, M. J., et al. *Gaussian 16, Revision A.03* (Gaussian, Inc., 2016)
49. Perdew, J. P. Density-functional approximation for the correlation energy of the inhomogeneous electron gas. *Phys. Rev. B* **33**, 8822–8824 (1986).
50. Becke, A. D. Density-functional exchange-energy approximation with correct asymptotic behavior. *Phys. Rev. A Gen. Phys.* **38**, 3098–3100 (1988).
51. Sheng, M., Jiang, N., Gustafson, S., You, B., Ess, D. H. & Sun, Y. A nickel complex with a biscarbene pincer-type ligand shows high electrocatalytic reduction of CO₂ over H₂O. *Dalton. Trans.* **44**, 16247–16250 (2015).

Figures

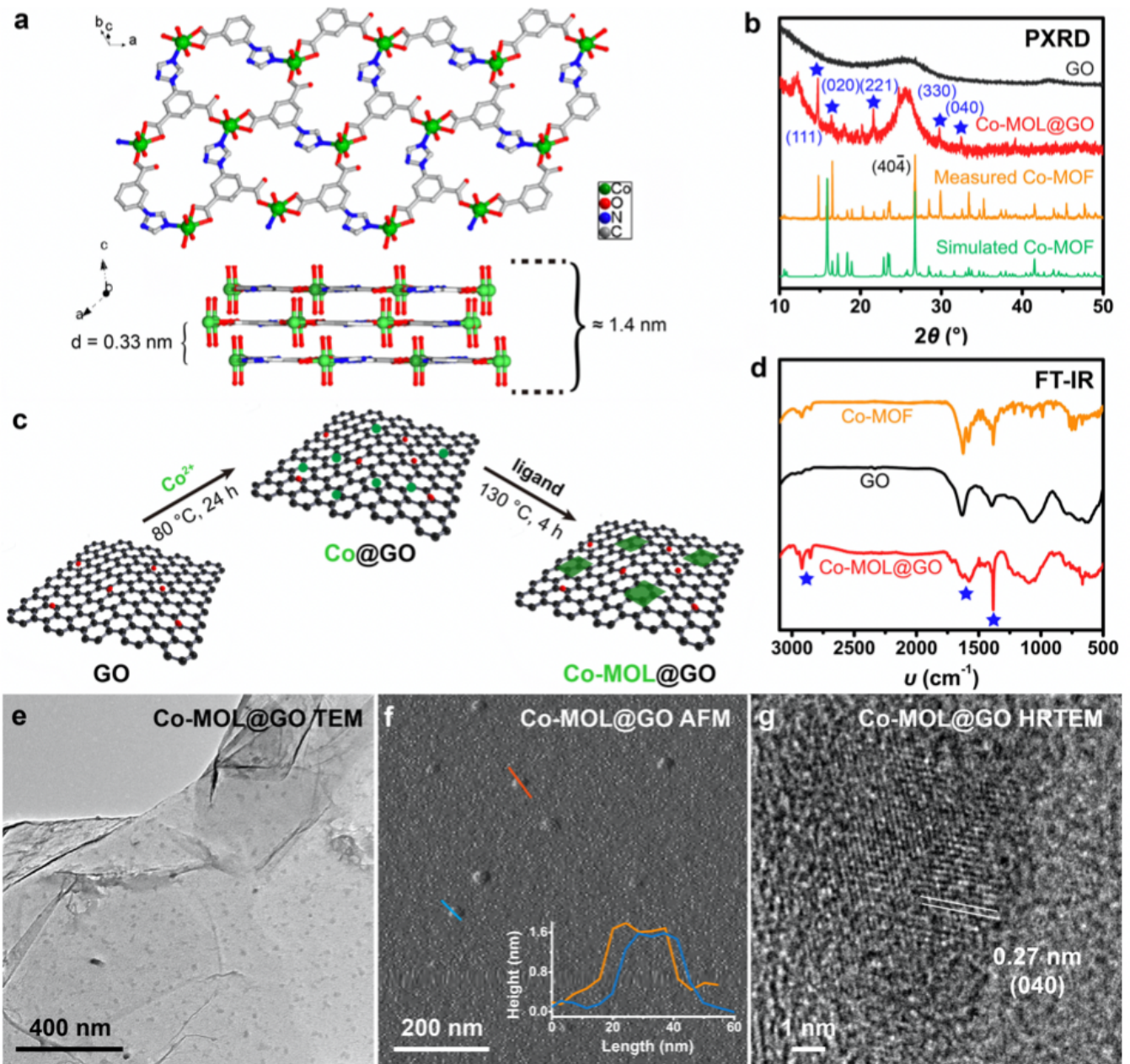


Figure 1

Synthesis and characterization. a Layer-like structure of Co-MOF. b PXRD patterns of Co-MOF, GO and Co-MOL@GO as well as simulated pattern of Co-MOF. c Synthesis of Co-MOL@GO. d FT-IR spectra of Co-MOF, GO and Co-MOL@GO. e TEM, f AFM and g HRTEM results of Co-MOL@GO. The blue stars in b and d highlight the matched signals between Co-MOF and Co-MOL@GO.

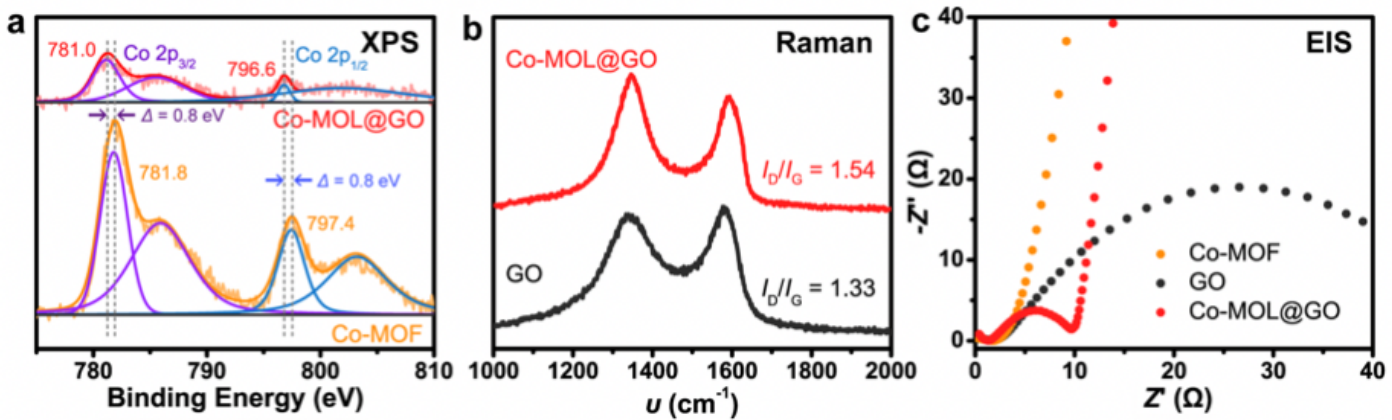


Figure 2

Comparison between Co-MOL@GO and Co-MOF. a Co 2p XPS spectra of Co-MOL@GO and Co-MOF. b Raman spectra of Co-MOL@GO and GO. c EIS spectra of Co-MOL@GO, GO and Co-MOF.

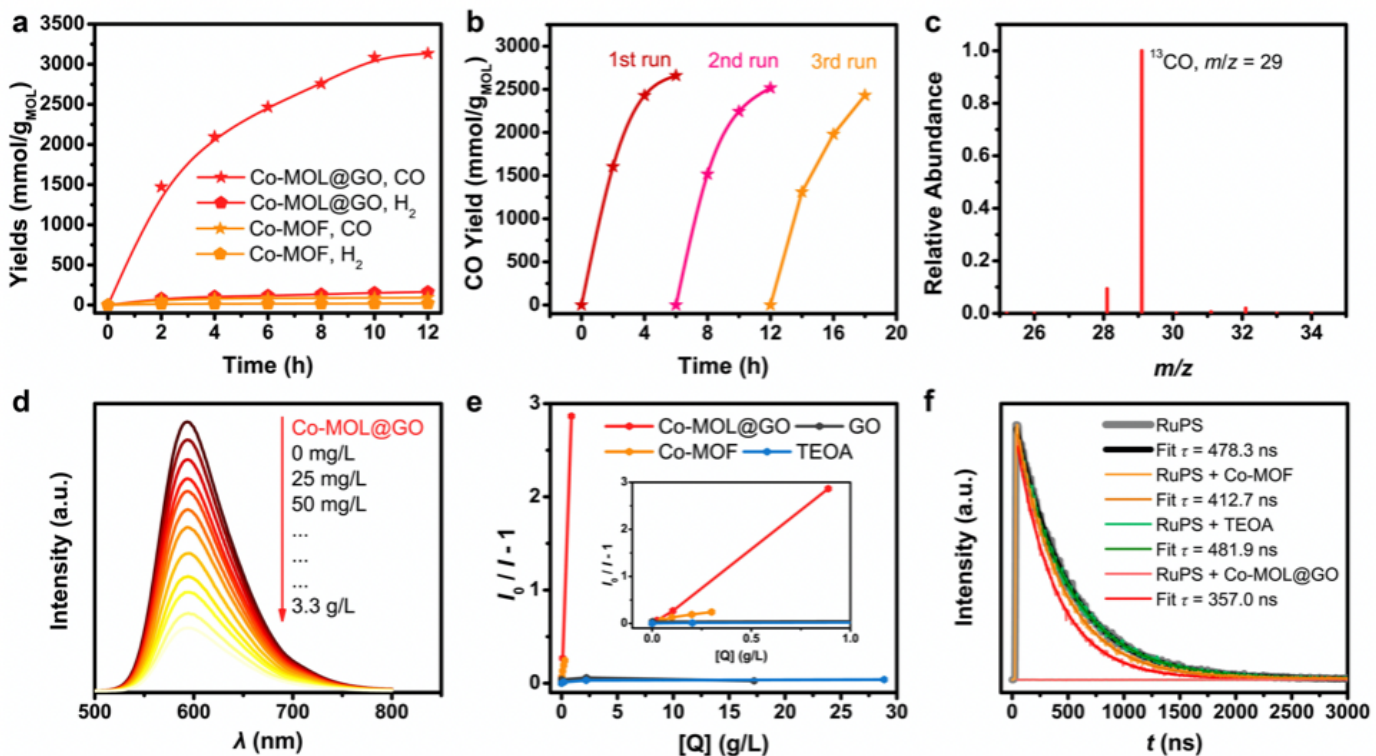


Figure 3

Photocatalytic CO₂ reduction. a Time profiles of CO and H₂ evolution catalyzed by 10 mg/L Co-MOL@GO and Co-MOF with the irradiation of a blue LED (450 nm) in CH₃CN/H₂O (v:v = 4:1) solution under 1 atm CO₂. b Recycle experiments of CO production with Co-MOL@GO as the catalyst. c ¹³CO₂ isotope labeling experiments. d Fluorescence spectra of a CH₃CN/H₂O (v : v = 4:1) solution containing 0.4 mM RuPS in the presence of 0~3.3 g/L of Co-MOL@GO with the excitation at 450 nm. e Stern-Volmer plot of fluorescence by the quenchers of Co-MOL@GO, Co-MOF and triethanolamine (TEOA) versus the mass

concentrations ([Q]). f Time-resolved absorption spectra of 0.4 mM RuPS (black), RuPS with 0.3 M of TEOA (green), RuPS with 50 mg/L of Co-MOF (orange) and RuPS with 50 mg/L Co-MOL@GO (red) in CH₃CN with the excitation wavelength of 450 nm.

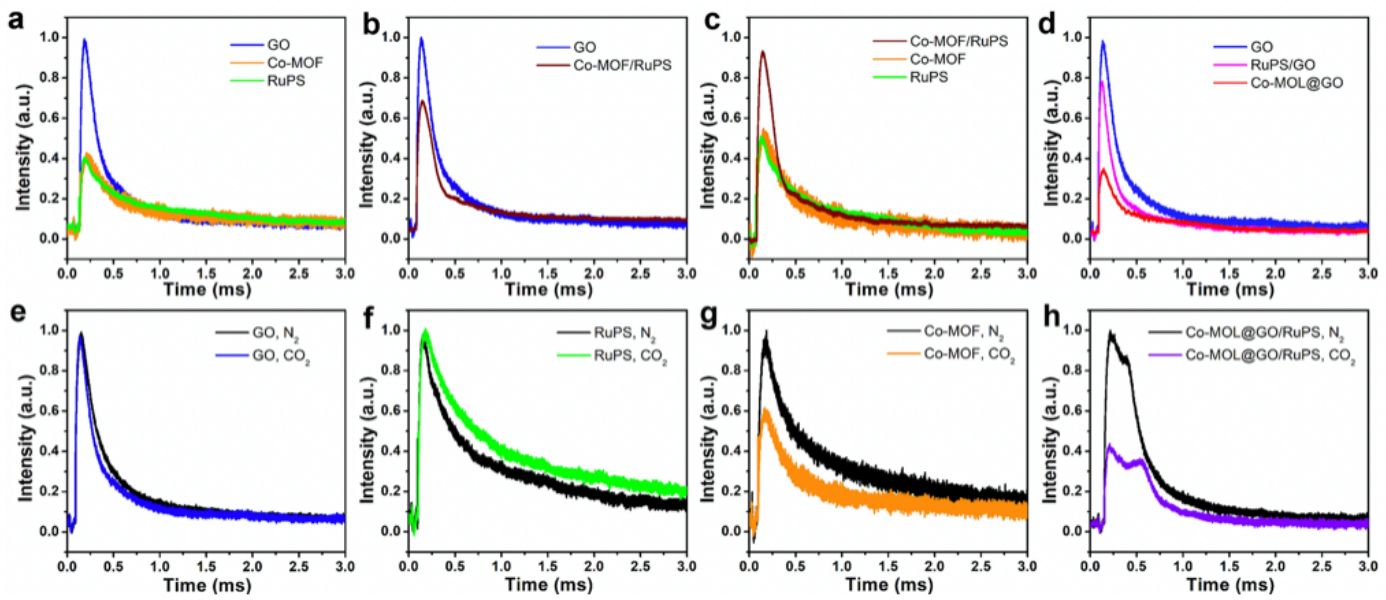


Figure 4

In situ transient photovoltage. Comparison of the in situ TPV curves among GO, Co-MOF and RuPS under N₂; b among Co-MOF/RuPS mixture, Co-MOF and RuPS under N₂; c between GO and Co-MOF/RuPS mixture under N₂; d among GO, RuPS/GO mixture and Co-MOL@GO under N₂. Comparison of the in situ TPV curves under N₂ or CO₂ with e GO, f RuPS, g Co-MOF or h Co-MOL@GO/RuPS mixture under N₂ or CO₂, respectively.

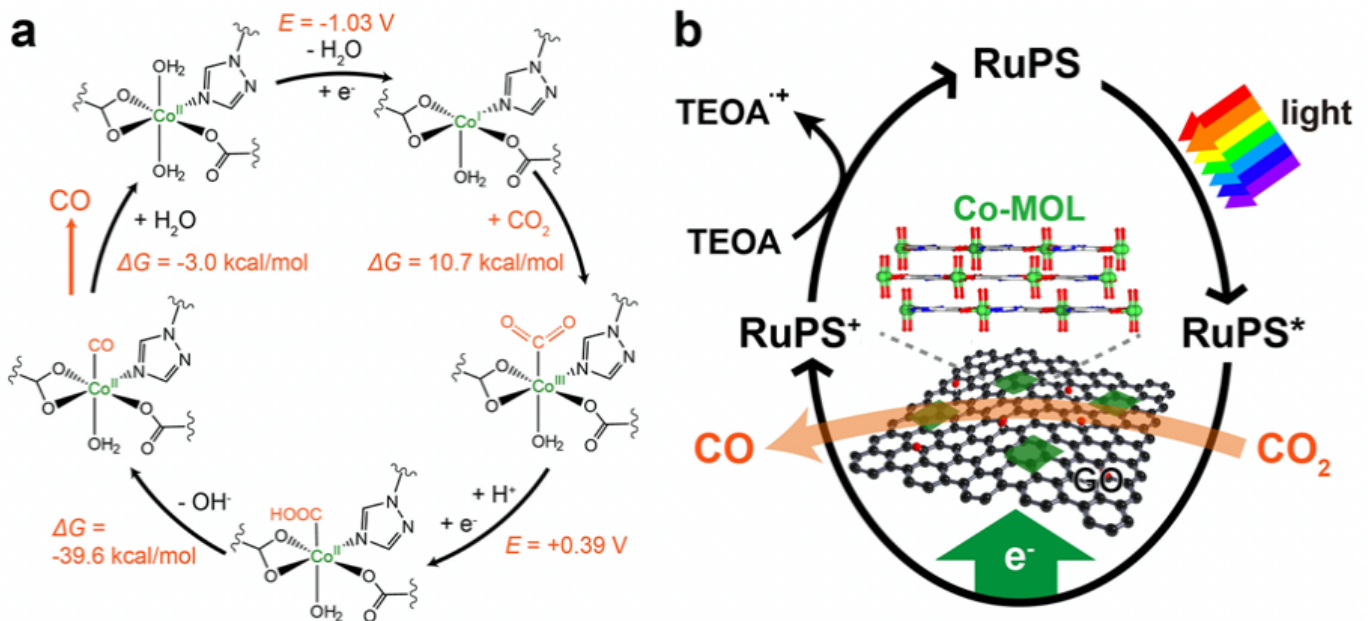


Figure 5

Proposed mechanisms. a Calculated mechanism with the molecular unit of Co-MOF for photocatalytic CO₂-to-CO conversion, showing the calculated redox potentials and free energy changes. b Proposed photocatalytic mechanism with Co-MOL@GO as the catalyst.

Supplementary Files

This is a list of supplementary files associated with this preprint. Click to download.

- SupportingInformation.doc